FABRICATION OF OPEN-PORE BIODEGRADABLE MAGNESIUM ALLOY SCAFFOLD VIA INFILTRATION TECHNIQUE

Abdurrahim Temiz and **Mustafa Yaşar**
Department of Industrial Design Engineering, Karabuk University, Karabuk, Turkey

Erkan Koç
Department of Biomedical Engineering, Karabuk University, Karabuk, Turkey

Abstract

A casting technology based on the infiltration method was used to fabricate a controllable porous Mg alloy structure. The porous structure was designed as a gyroid structure, which is one of the well-known triply periodic minimal surface structures. The model used as a placeholder was produced in a stereolithography apparatus and embedded in NaCl as a mold. In order to define the mechanical properties, sheep bone was cut to the same size as the gyroid structure and these were then analyzed under compression loads. The compression test results were compared with each other and with the Young's moduli of human trabecular bone as stated in the literature. The results of the compression tests indicated that the Young's modulus of the gyroid structure obtained from experimental data was in the range of the Young's moduli of human trabecular bone but lower than the Young's modulus of the sheep bone obtained from the experimental data. A finite element model of the gyroid structure was designed using the LS-Dyna module in ANSYS Workbench and validated with experimental test results. In addition, finite element analysis of the circular cross-sectional beam was also carried out and compared with the gyroid structure in order to evaluate the deformation and fractures.

Graphic Abstract
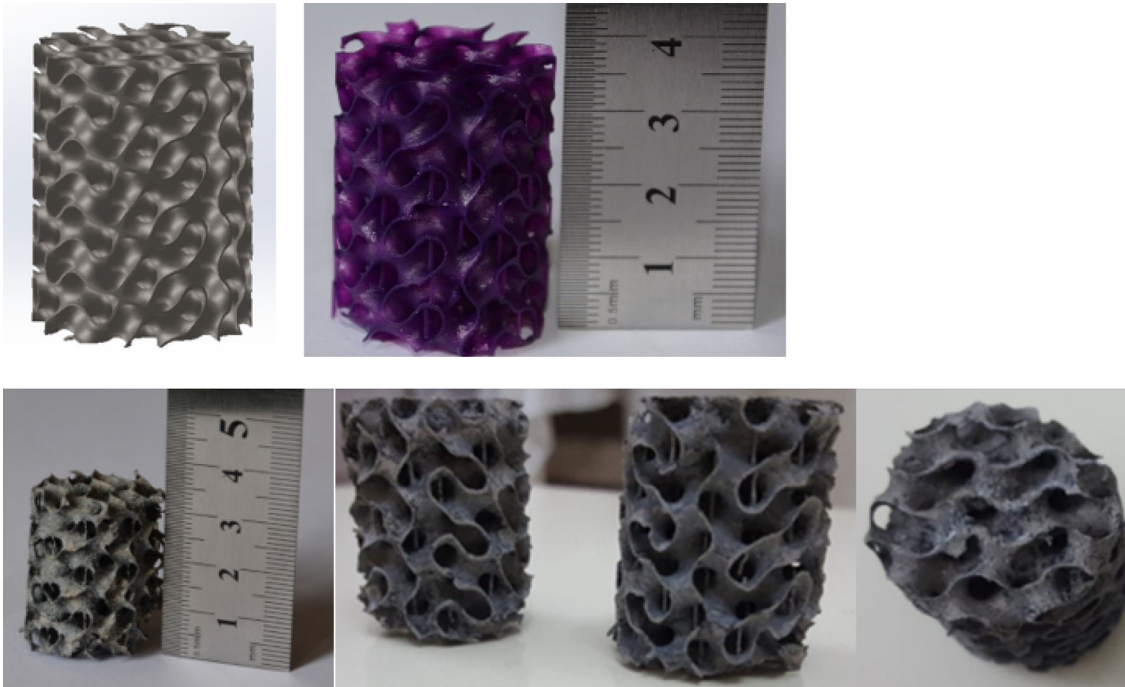
Keywords: *gyroid, infiltration, casting, porous structure, stereolithography apparatus (SLA)*

Introduction

Over four thousand years ago, metallic implants were the earliest biomaterials used to repair skull defects during cranioplasty in 2000 BC.[1] Metals are better suited for load-bearing applications compared to ceramic or polymeric materials in terms of fracture toughness and high strength.[1–5] Metallic biomaterials, including stainless steels, cobalt-chromium-based alloys, and titanium, are currently approved and widely used; however, their use leads to inflammatory cascades that reduce biocompatibility and bring on tissue loss. Furthermore, the Young's modulus of existing metallic biomaterials does not correspond well to that of natural bone. This causes stress-shielding that triggers bone resorption, increased porosity in the bone surrounding the implant, delayed bone healing, and loosening of the implant.[2,4–10] Although bioinert implants are successful in bone fixation applications, there are also some inevitable problems when they remain permanently in the human body. In the human body, biodegradable implant materials can gradually be dissolved, absorbed, consumed, or excreted.[5] Various clinical trial results have shown that biodegradable Mg alloys exhibit acceptable mechanical properties and good biocompatibility and biodegradability.[9,11–13]

In the past, porous metal implants have been widely used to improve the bone-implant interface. These porous structures can prevent loosening of the implant and encapsulation.[14] In addition, they have a very high potential in biomedical applications as scaffolds in terms of promoting bone ingrowth, cell migration, and in reducing stress shielding.[15] To further stimulate tissue ingrowth[16,17] and to adapt the density distribution to meet the specific strength, modulus, and deformation requirements during implantation, one approach would be to use porous materials[4,12] The Young's modulus of these super-light porous structures is closer to that of natural bone, thus minimizing implant loosening and stress shielding.

Metallic cellular materials can be produced by the dynamic gas injection method,[18–21] chemical vapor deposition,[18,22] powder metallurgy,[18,23,24] casting with space holders,[18,24–26] or metallic additive manufacturing (AM).[1]

Table 1. Chemical Composition of the Mg Alloy AZ91

Alloy	Composition wt%			
	Al	Zn	Mn	Mg
AZ91	8.50	0.80	0.20	Balance

However, it is acknowledged by the scientific community that magnesium alloys are very reactive, and therefore must be handled under extremely protective conditions during casting or sintering. Wen et al. developed an open-cell Mg foam using powder metallurgy with space holder technology.[16] Körner et al. proposed adding a blowing agent to the melt during the thixomolding process to produce a closed-cell Mg foam.[27] Renger and Kaufmann produced closed-cell Mg alloy foam using the vacuum foaming method.[28] Mehara et al. produced a closed-cell Mg foam via the precursor method using machined chips.[13] Yang et al. obtained Mg foam using the blowing agent method. They used a mixed atmosphere of CO_2 and SF_6 to shield the Mg alloy melt from reactions.[29] Hao et al. produced Mg foams by the powder metallurgy manufacturing process with space holding particles in an Ar atmosphere as a protective gas.[30] Neu et al. produced closed-cell Mg and Mg alloy foam via powder metallurgy in an Ar atmosphere using precursors with and without a blowing agent.[31] Fabrizio et al. obtained an Al–Si–Mg foam using a hydraulic cylinder to generate the infiltration pressure.[32] Aghion and Perez obtained MRI 201S Mg alloy foams using space holders in an Ar atmosphere as a protective gas.[33] Yilong et al. produced Mg foam using powder metallurgy with a space holder technique[34] Lara-Rodriguez et al. obtained open-cell Mg and Mg alloy foams using the replication method via infiltration.[35] Sivashankari and Krishnamoorthy produced Mg alloy foam using powder metallurgy with a blowing agent. In this method, the conditioning of the atmosphere involves removing the air from the reaction chamber and replacing it with an inert atmosphere, typically Ar. However, except for metallic additive manufacturing (AM), producing porous structures in controllable geometries is still a challenge.

Triply periodic minimal surfaces (TPMS) have been recently introduced and are provoking interest as attractive candidates for the design of bio-morphic scaffold structures.[36–38] Since the gyroid surface has no reflection symmetry or straight lines, it exhibits a topology similar to human trabecular bone. This enables reduction of the effect of stress concentration within the structure and provides highly efficient mechanical properties compared to space-frame truss structures.[36,37] Recently, Yan et al. examined the manufacturing of TPMS scaffolds and demonstrated that TPMS scaffolds with 80–95% porosity had an elastic modulus in the ranges of 0.12–1.25 Gpa, which was a good match with cancellous bone.[39] Li et al. reported that the gyroid had potential for orthopedic bone replacement.[40]

In this study, an open-pore, lightweight TPMS porous gyroid structure was designed and fabricated as an Mg alloy foam. The presented model was produced via 3D stereolithography (SLA). Compression tests were performed on the gyroid structure and on sheep bone in the same size as the gyroid structure. These results were compared with each other. The main hypothesis was that porous Mg gyroid structures could be obtained by using casting technology. Using a Mg alloy gyroid structure having a tailored Young's modulus as a scaffold or implant might solve the stress shielding problem.

Experimental Procedures

Specimen Manufacturing

The material used in this study was the AZ91 Mg alloy, which is one of the most widely used biodegradable alloys. The chemical composition of the Mg alloy AZ91 is shown in Table 1.

Casting with an infiltration technique was used to prepare the Mg alloy gyroid structure. First, the geometry design of the gyroid structure was carried out. A cylindrical gyroid structure was designed similar in size (mean diameter, 25
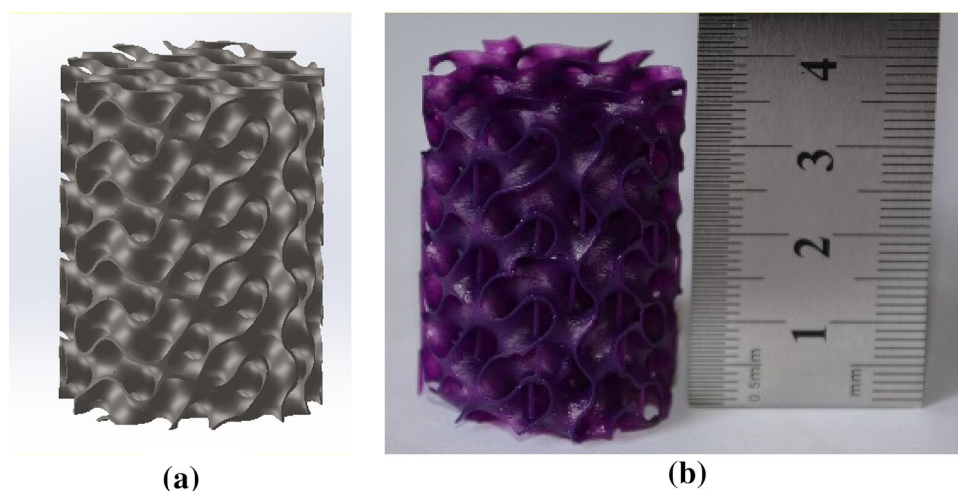
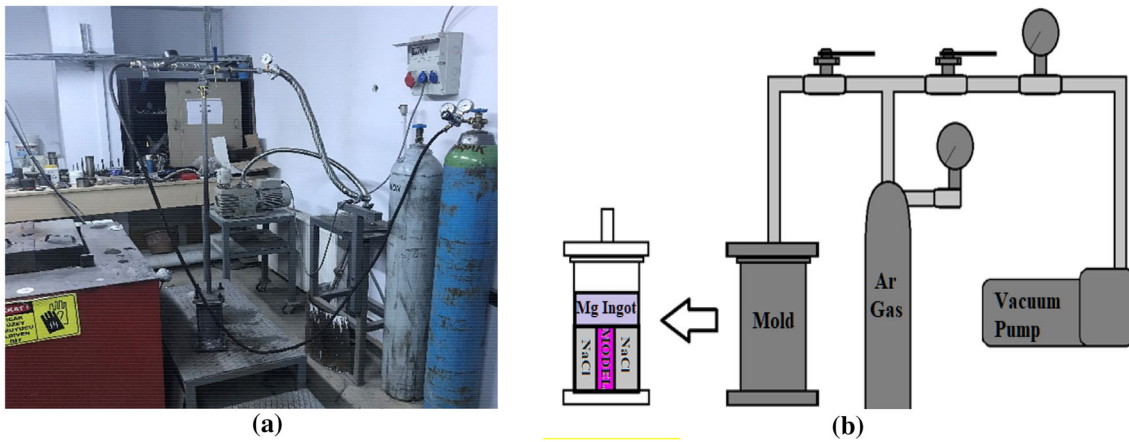**Figure 1. Gyroid structure: (a) CAD model, (b) SLA-manufactured model.**

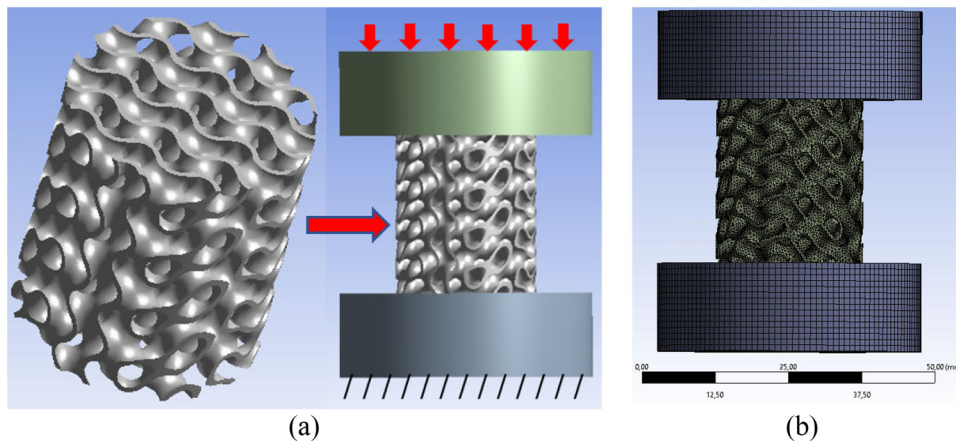**Figure 2. Casting system: (a) real image, (b) schematic view.**

Figure 3. (a) Boundary condition and (b) mesh of the analysis.

**Table 2. Imput Material Elastic Properties and Failure**

Density (ρ)	Young's modulus (E)	Poisson's ratio (ε)	Failure (max. equivalent plastic strain EPS)
1.8 g/cm³	45,000 MPa	0.35	0.25

mm; height, 30 mm) to the sheep bone used for the compression test. The gyroid unit wall surfaces were generated using the Surface Design Module in Solidworks software (Dassault Systems Inc., USA). The unit wall surface was then assembled and the desired thickness was given to the surface body in the same software. The gyroid structures were designed with angles between the struts and the axial direction of 45°. An SLA was then used to create wax casting models. Because of its ability to produce complex part geometries, additive manufacturing (AM) enables the production of molds, cores, and models.[41-46] For SLA, the three dimensional (3D) computer-aided design (CAD) file was cut into 25-μm layers using PreForm software

(Formlabs Inc., Somerville, USA). The casting model was then fabricated layer-by-layer using the Form 2 SLA 3D printer (Formlabs Inc., Somerville, USA) from Castable Wax Resin (Formlabs Inc., Somerville, USA) specially made for investment casting. The resin degrades completely at 700 °C under air atmosphere.[47] The CAD model of the gyroid structure and the SLA-manufactured model of the gyroid structure are shown in Figure 1.

The casting models were then embedded and manually pressed in a mixture containing 98% NaCl and 2% phenol novolac epoxy resin. The casting was carried out in the system used for the replication process.[35] The real casting system and schematic view of the casting system are shown in Figure 2. The melting was done under vacuum (10^{-5} mbar) in a 304 series steel mold to prevent reactions.

Before the mold was put into the furnace, the permanent mold chamber was evacuated, filled with argon and evacuated a second time. This process was repeated three times. When the furnace reached 400 °C, the mold in which the Mg ingots were placed was put into the oven and properly sealed. The vacuum valve was kept open during the
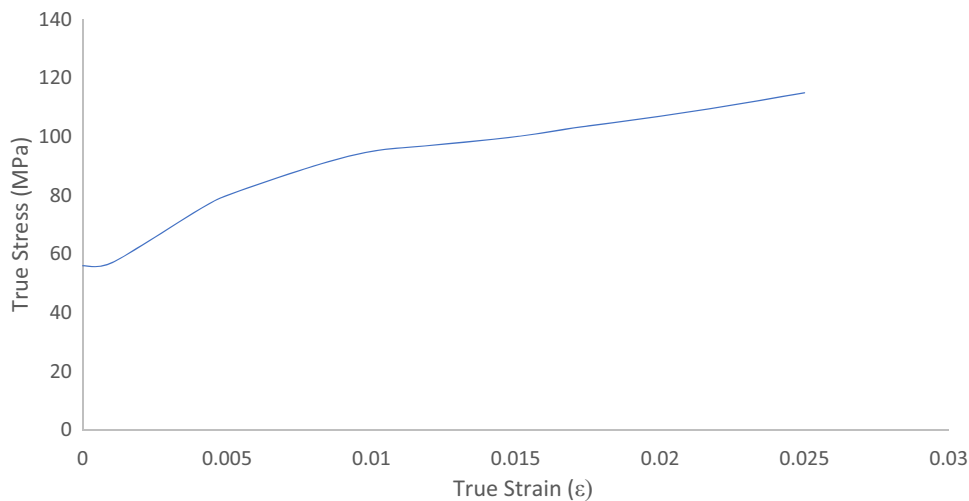
Figure 4. Plastic behavior of AZ91 magnesium alloy.
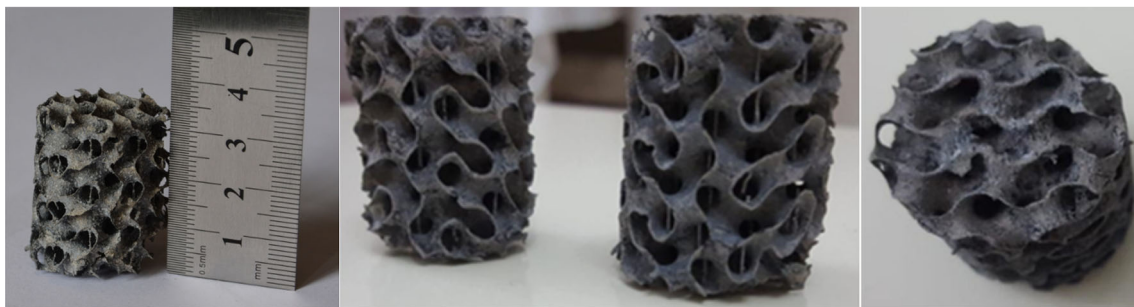
Figure 5. Typical macroscopic morphology of the Mg gyroid scaffold.

melting process. The furnace was heated up to 730 °C and maintained at this temperature for 45 min. During the sintering process of the NaCl, the model was burned out when casting the scaffolds with AZ91, respectively. Because the casting model form was removed during heating, the NaCl mold had a porous structure. Since molten Mg alloy could not flow through the narrow routes in the porous mold naturally, it was forced forward using Ar gas at 2 bar. In the next stage, the mold was cooled to room temperature. Finally, the mold material (NaCl) was dissolved afterward using water, leaving the open-cell Mg alloy. A magnetic stirrer hot plate was used at 700 rpm in water tanks at 90 °C, with the intent of a better dissolution performance. When all the NaCl was dissolved, the Mg foam gyroid scaffold was dipped in HCl and washed with ethanol.

Table 3. Average Pore Size, Wall Thickness, and Porosity of the Gyroids

	Pore size (mm)	Wall thickness (strut size) (mm)	Porosity
Designed	3	0.25	88.87
SLA	2.8	0.26	86.66
Casting	2.7	0.27	83.92

Finite Element Analysis

The finite element analysis of a gyroid model having the same dimensions as the manufactured specimen was carried out on the LS-Dyna module in ANSYS Workbench. A model was established consisting of a gyroid geometry sandwiched in-between a top and bottom die. The explicit mesh physics preference was selected with 118432 nodes and 193969 elements and the patch-independent finite element method (FEM) was used. The boundary condition and mesh of the analysis is displayed in Figure 3. The bottom die was fixed and the top one moved down by using displacement until it reached half of the dimensions of the specimen.

The imput material elastic properties and failure for AZ91 are shown in Table 2.[48] The flow stress curve was fitted for characterization of the plasticity.

A multi-linear isotropic hardening model was used for nonlinear analysis to fit the flow stress curve. The flow stresses are shown in Figure 4.[48]

In addition, the circular cross-sectional beam model used by Maier et al. in their study[4] was designed in the same bulk and pore dimensions as the gyroid model. The finite

element analysis of the circular cross-sectional beam was also carried out under the same boundary conditions on the LS-Dyna module in ANSYS Workbench in order to show deformation evolution and the fractures.

Results and Discussion

The relative density of a porous structure is the most important structural property influencing the Young's modulus (E). In porous materials, the relationship of relative density with elastic modulus and porosity with relative density is expressed in the following equations, respectively.[12]

$$E/E_s = C(\rho/\rho_s)^2 \qquad \text{Eqn. 1}$$
$$p = 1 - \rho/\rho_s \qquad \text{Eqn. 2}$$

In the equations, E is the elastic modulus of metal foam, E_s is the elastic modulus of solid metal, C is a constant of about 1, ρ is the density of the foam, ρ_s is the density of the solid material, and p is the porosity.

Mg Alloy Scaffold Structure

The typical macroscopic morphology of the Mg scaffold is shown in Figure 5. It can be seen that the pores are almost the same as those in the model produced via the SLA machine, which just copies out the shape and the cell sizes of the model. The morphology of the pores and the controllability of their size can be seen in the figure. Controllable geometries having different porosity sizes can also be obtained by changing the shape of the model produced by the SLA printer. However, the wall thickness or strut size of the manufactured foam was slightly different from that of the model since the NaCl mixture could not be compressed sufficiently on the model and the Mg alloy melted due to the HCl used during post-production NaCl removal.

A cylindrical gyroid scaffold was manufactured similar in size (mean diameter, 25 mm; height, 30 mm) to the sheep bone used for the compression test. All of the scaffolds had interconnected porous structures. Table 3 presents the

average porosity, pore size, and wall thickness or strut size of the gyroids.

The average porosity, pore size, and wall thickness or strut size of the gyroid structure were 83.92%, 3 mm, and 0.25 mm, respectively, in the casting structure. Although the surface of the walls (struts) was rough, their framework was well-defined and continuous. The difference between the designed, the SLA, and the casting results was due to the internal supports. When producing the model using SLA, the supports (which are a very important aspect of complicated 3D printing models) in the inner parts affected the porosity. The molten metal filled all the walls (struts), including the supports.

Compressive Test and Finite Element Model Validation

The mechanical properties of the Mg alloy gyroid scaffold were analyzed via compression tests. The sheep bone (without separating the cortical and cancellous parts) was also used in the compression tests by cutting it to approximately the same size (mean diameter, 25 mm; height, 30 mm) as the manufactured controllable gyroid scaffold. The compression tests were performed on the sheep bone in order to compare the results with those of the developed structure because the mechanical properties of sheep bone are closest to those of human bone and sheep bone is more easily accessed than human bone. The sheep bone under compression testing is shown in Figure 6.

Compression tests were carried out on the Zwick/Roell 600 kN mechanical testing device. The compression test of the gyroid structure was carried out for up to 50% of its length. The compression test of the sheep bone was completed when the sheep bone fractured. The deformation evolution of the gyroid model under compression is shown in Figure 7.

The force-deformation curves of the gyroid scaffold and sheep bone are shown in Figure 8. The force-deformation curve obtained via FEM was also evaluated with the reported experimental results.
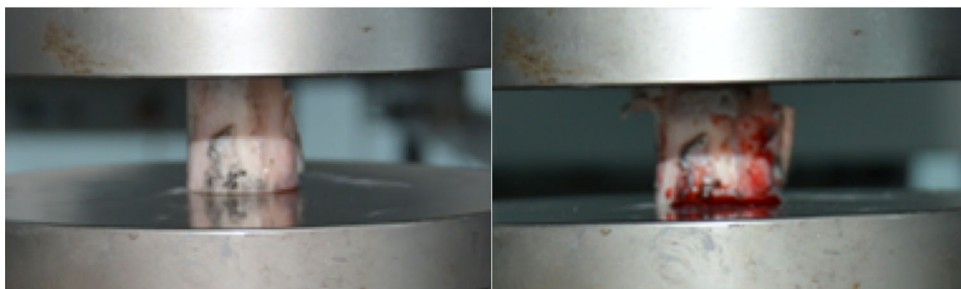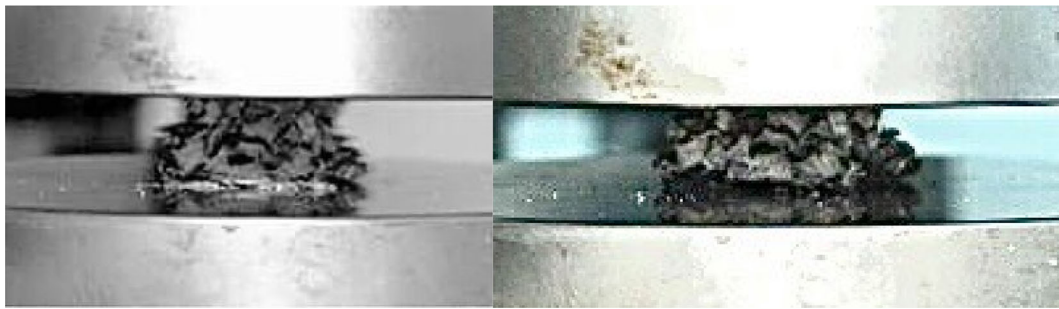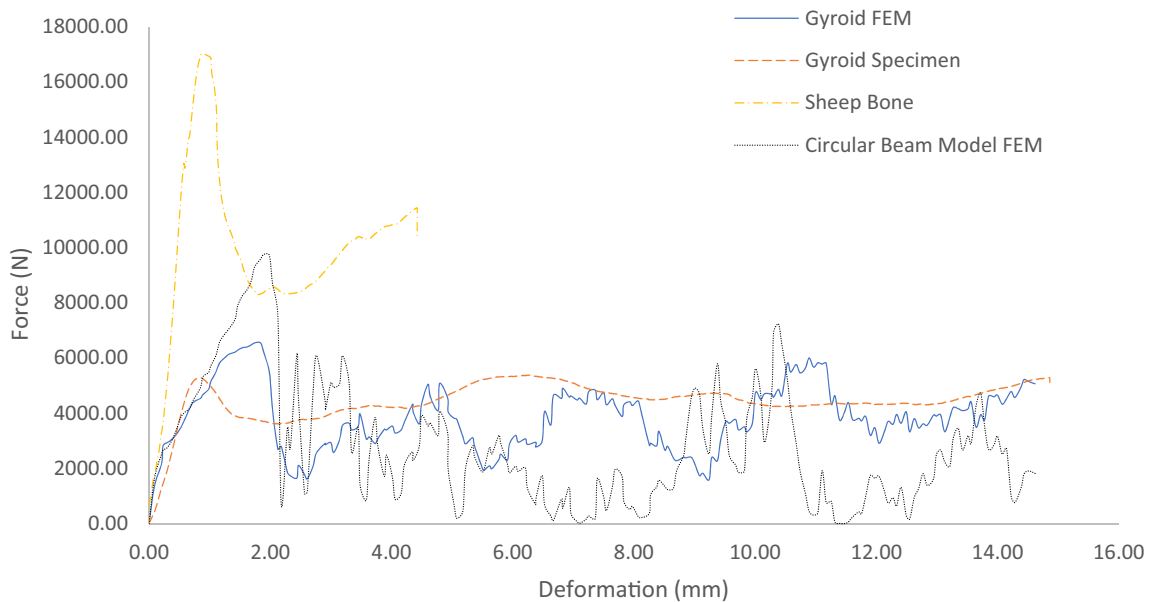

Figure 6. Sheep bone under compression testing.

Figure 7. Deformation evolution of gyroid model under compression testing.


Figure 8. Comparison of experimental and finite element model force-deformation curves.

As seen in Figure 8, the gyroid curve presents the typical compressive properties of porous structures, such as, an elastic deformation stage at the beginning of deformation and a rather long plateau stage as well as constant low stress to large strain. The serrated plateau represents the brittle deformation mode, i.e., brittle fracture of the strut after the yield. The force-deformation curves for FEM also showed a similar evolutionary trend and an overall good agreement with the experiment results. The max force values of the gyroid structure from the experimental data and FEM were 5378.49 N and 6544.6 N, respectively. The max force values of the sheep bone and the circular cross-sectional beam model were 17008.94 N and 9752.1 N, respectively. The Young's modulus of the gyroid structure obtained from the experimental data using regression methods and the theoretical calculation using Eqn. (1) were 477.68 MPa and 14.104 GPa, respectively. The Young's modulus of the gyroid structure obtained from the experimental data was within the range of the Young's moduli of human trabecular bone (0.050 to 3.2 GPa).[21] When compared with the sheep bone, the gyroid structure had a lower Young's modulus (1733.88 MPa), whereas the yield stress

of the sheep bone was about three times higher. However, the yield stress of the gyroid structure was sufficient to carry the weight of an average person (75kg). Moreover, it can be seen from the compression graph in Figure 7 that the manufactured gyroid structure exhibited good energy absorption. The deformation evolution of the gyroid model under compression obtained from FEM is shown in Figure 9.

As shown in Figure 9, in the FEM results, the gyroid specimen finally entered a spherically uniform failure mode during the compression process, showing the bending of the cell walls and outward convexity in the central part. During the compression test, the gyroid structure exhibited a trend similar to that of the experimental results. The fractures in the specimen were also similar to those in the experiment. The deformation evolution of the circular cross-sectional beam model under compression obtained via FEM is shown in Figure 10.

The deformation evolution and the fractures of the circular cross-sectional beam model are different from those of the
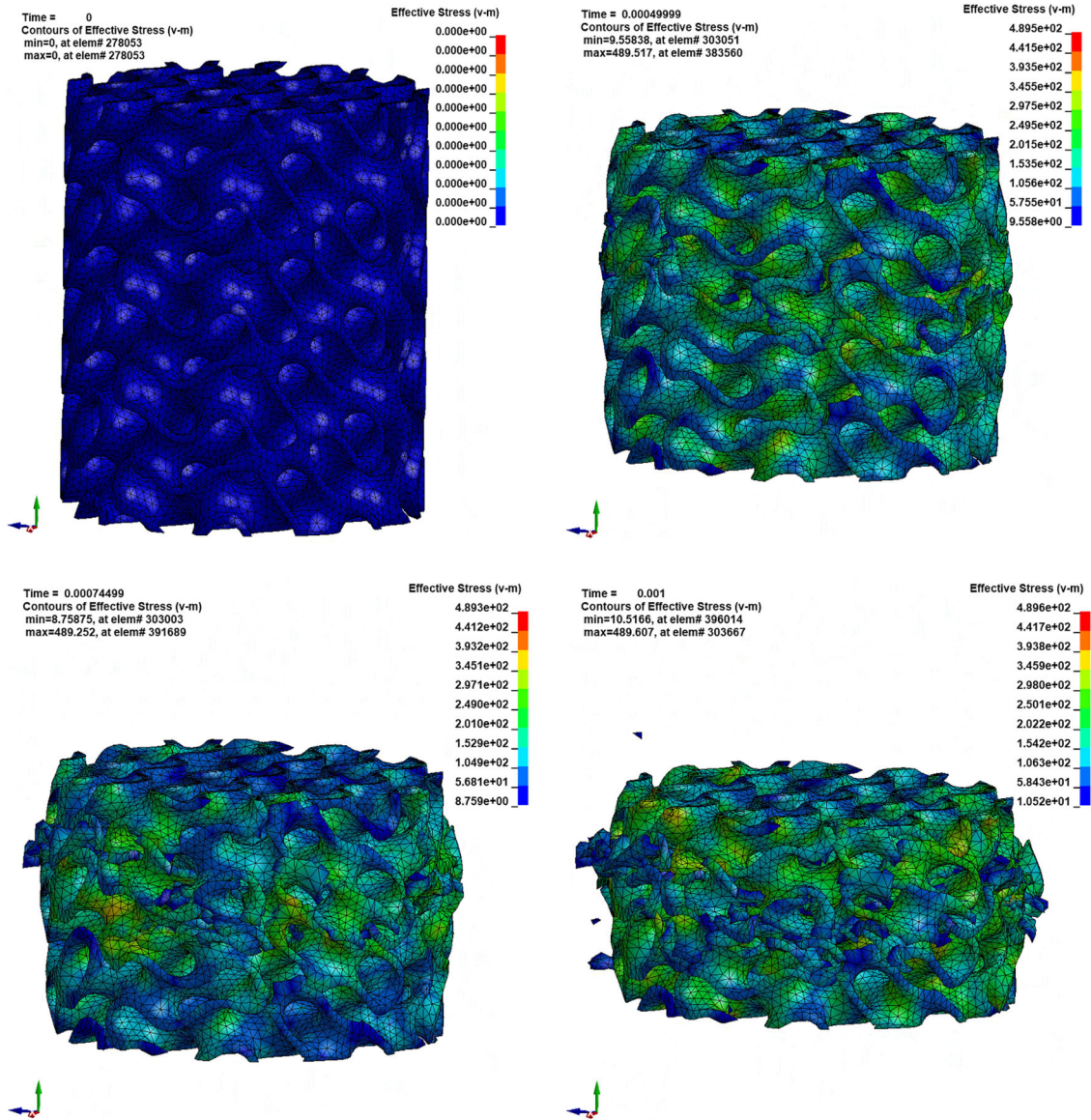
Figure 9. Simulation results of deformation evolution of the gyroid model under compression.

gyroid model. The fractures start in the inner regions in the circular cross-sectional beam model. The circular cross-sectional beam model exhibited less bending of the cell walls and outward convexity in the central part compared to the gyroid model in the FEM results.

Conclusion

In this study, a gyroid-type triply periodic minimal surfaces (TPMS) biodegradable structure was utilized to produce a porous structure via casting. Compression tests were carried out on the produced gyroid structure and on sheep bone and the results were compared. A finite element model of the gyroid structure was also created using the LS-Dyna module in ANSYS Workbench. The main conclusions drawn from this study are as follows.

1. Casting technology based on the infiltration method could be used successfully to manufacture open-cell Mg foam. A controllable geometry could be achieved by using a model produced from castable resin via SLA.

2. The Young's modulus of the gyroid structure obtained from the compression test using regression methods was 477.68 Mpa, which is within the range of the Young's moduli of human trabecular bone (0.050 to 3.2 GPa) as stated in the literature. Moreover, the Young's modulus of sheep bone (17008.94 MPa) obtained from the compression test using regression methods was
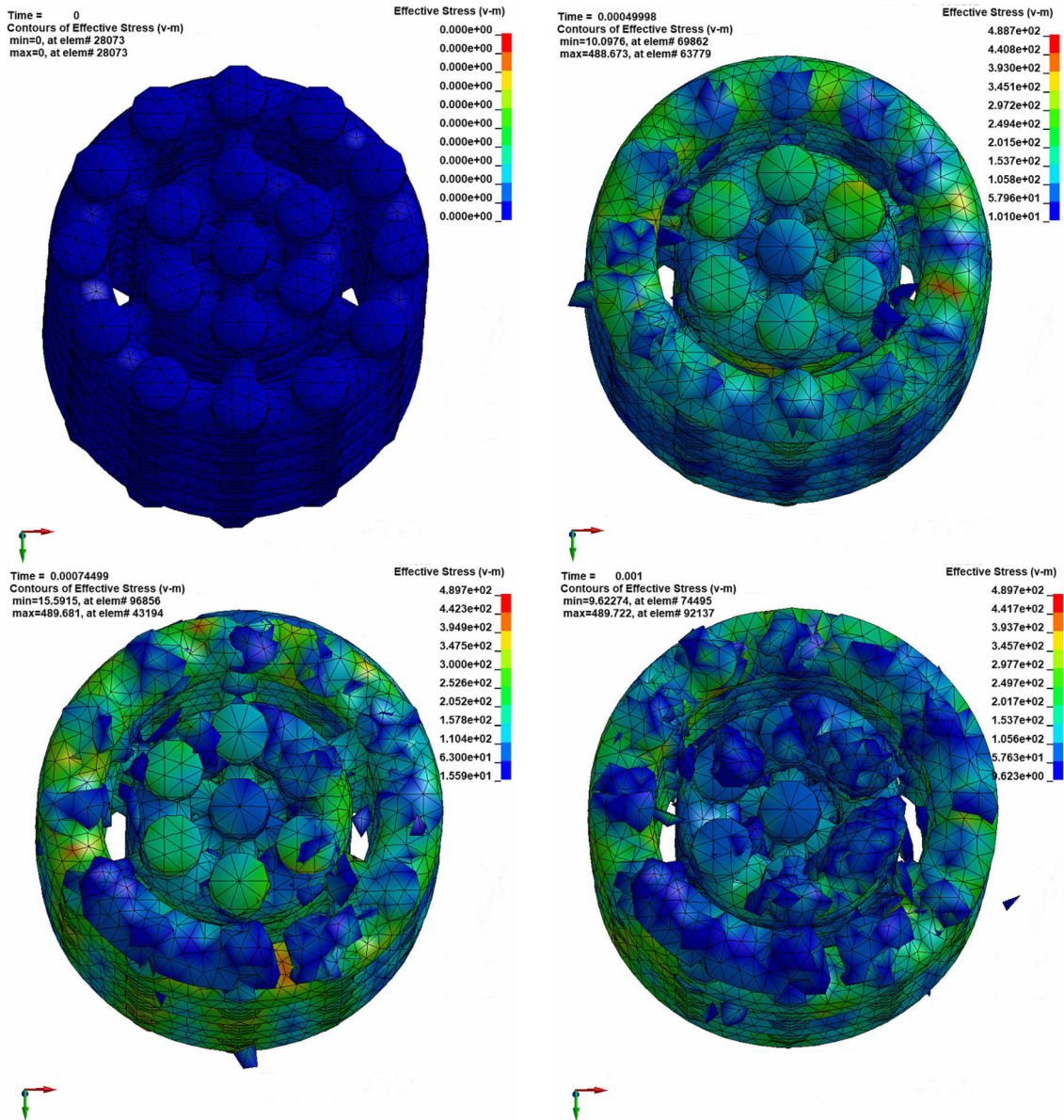
Figure 10. Simulation results of deformation evolution of the circular cross-sectional beam model under compression.

higher than that of the gyroid structure (477.68 MPa). Using this Mg gyroid structure having a compatible Young's modulus as a scaffold or implant might be the solution to the stress shielding problem. However, although the compression test results demonstrated that the yield stress of the gyroid structure was approximately three times lower than that of sheep bone, it can carry much greater weight than that of the average human (75kg). In addition, the yield stress of this structure could be increased by increasing the strut thickness. The Young's modulus could be tailored based on the design of the gyroid, which could be varied spatially and made more complex. The structure could then be customized in terms of the Young's modulus to match the type of bone for which it was needed.

3. Mg foam may be a promising candidate for energy-absorbing applications because its force-deformation curves display a rather long plateau region with a smaller plateau of stress. The composition of the foam is 73.92% porosity, with an average pore size and wall thickness (strut size) of 3 mm and 0.25 mm, respectively.

4. The process needs further optimization, especially in terms of pore size and porosity. However, the results clearly showed that models produced from castable resin using NaCl as a mold have great potential for controllable porous

structure formation. In addition, as a mold, NaCl can easily be removed, leaving a porous scaffold.

5. A finite element model was designed and validated on the LS-Dyna module in ANSYS Workbench. In the gyroid model, under normal conditions, the onset of fracture was initiated in the central region, as was expected. During the compression process, the FEM gyroid specimen in the final spherically uniform failure mode displayed bending of the cell walls and outward convexity in the central part. During the compression test, the experimental results of the gyroid structure showed a similar trend. The fractures were also similar to those of the experimental specimens. The max force values of the gyroid structure from the experimental data and the FEM were 5378.49 N and 6544.6 N, respectively.

6. Finite element analysis of the circular cross-sectional beam was also carried out under the same boundary conditions and compared with the gyroid structure. According to the results obtained from the FEM analysis, when the circular cross-sectional beam model was examined, the fractures were seen to start in the inner regions. The circular cross-sectional beam model exhibited less bending of the cell walls and outward convexity in the central part compared to the results of the FEM gyroid model. The finite element model could be used to perform further analyses for porous structures. The max force of the circular cross-sectional beam model was 9752.1 N, which was higher than that of the gyroid model. However, local minimum values of the gyroid model were higher than those of the circular cross-sectional beam model. Hence, the gyroid model displayed better energy absorption than the circular cross-sectional beam model.

REFERENCES

1. R. Singh, P. Lee, R. Dashwood et al., Titanium foams for biomedical applications: a review. Mater. Technol. **25**, 127–136 (2010). https://doi.org/10.1179/175355510X12744412709403

2. M.P. Staiger, A.M. Pietak, J. Huadmai et al., Magnesium and its alloys as orthopedic biomaterials: a review. Biomaterials **27**(9), 1728–1734 (2006). https://doi.org/10.1016/j.biomaterials.2005.10.003

3. S. Lascano, C. Arévalo, I. Montealegre-Melendez et al., Porous titanium for biomedical applications: evaluation of the conventional powder metallurgy frontier and space-holder technique. Appl. Sci. **9**(5), 982 (2019). https://doi.org/10.3390/app9050982

4. H.J. Maier, S. Julmi, S. Behrens et al., Magnesium alloys for open-pored bioresorbable implants. JOM (2020). https://doi.org/10.1007/s11837-020-04078-8

5. G. Song, Control of biodegradation of biocompatable magnesium alloys. Corros. Sci. **49**(4), 1696–1701 (2007). https://doi.org/10.1016/j.corsci.2007.01.001

6. K. Kato, S. Ochiai, A. Yamamoto et al., Novel multilayer Ti foam with cortical bone strength and cytocompatibility. Acta Biomater. **9**(3), 5802–5809 (2013). https://doi.org/10.1016/j.actbio.2012.11.018

7. O. Cetinel, Z. Esen, B. Yildirim et al., Fabrication, morphology analysis, and mechanical properties of Ti foams manufactured using the space holder method for bone substitute materials. Metals **9**(3), 340 (2019). https://doi.org/10.3390/met9030340

8. Y. Torres, J. Pavón, P. Trueba et al., Design, fabrication and characterization of titanium with graded porosity by using space-holder technique. Proc. Mater. Sci **4**, 115–119 (2014). https://doi.org/10.1016/j.mspro.2014.07.610

9. J.M. Seitz, A. Lucas, M. Kirschner, Magnesium-based compression screws: a novelty in the clinical use of implants. JOM **68**(4), 1177–1182 (2016). https://doi.org/10.1007/s11837-015-1773-1

10. D. Yang, Z. Guo, H. Shao et al., Mechanical properties of porous Ti–Mo and Ti–Nb alloys for biomedical application by gelcasting. Procedia Engineering **36**, 160–167 (2012). https://doi.org/10.1016/j.proeng.2012.03.025

11. H. Zengin, Role of Sr in microstructure, hardness and biodegradable behavior of cast Mg–2Zn–2Ca–0.5Mn (ZXM220) alloy for potential implant application. Int. Metalcast. **14**, 442–453 (2020). https://doi.org/10.1007/s40962-019-00366-5

12. X.Z. Lu, C.P. Lai, L.C. Chan, Novel design of a coral-like open-cell porous degradable magnesium implant for orthopaedic application. Mater. Des. **188**, 108474 (2020). https://doi.org/10.1016/j.matdes.2020.108474

13. K. Mehara, M. Kobashi, N. Kanetake, Fabrication of magnesium foam by precursor method using machined chips. Adv. Mater. Res. **26**, 905–908 (2007). https://doi.org/10.4028/www.scientific.net/AMR.26-28.905

14. S. Kashef, A. Asgari, T.B. Hilditch et al., Fracture toughness of titanium foams for medical applications. Mater. Sci. Eng. A **527**(29–30), 7689–7693 (2010). https://doi.org/10.1016/j.msea.2010.08.044

15. L.M.R.D. Vasconcellos, M.V.D. Oliveira, M.L.D.A. Graça et al., Porous titanium scaffolds produced by powder metallurgy for biomedical applications. Mater. Res. **11**(3), 275–280 (2008). https://doi.org/10.1590/S1516-14392008000300008

16. C.E. Wen, Y. Yamada, K. Shimojima et al., Compressibility of porous magnesium foam: dependency on porosity and pore size. Mater. Lett. **58**(3–4), 357–360 (2004). https://doi.org/10.1016/S0167-577X(03)00500-7

17. V. Lopes, H. Puga, J. Barbosa et al., Effect of yttria mould coating on the investment casting of AZ91D-1 wt% CaO magnesium alloy. Int. Metalcast. **14**, 98–107 (2020). https://doi.org/10.1007/s40962-019-00339-8

18. V.H. Carneiro, S.D. Rawson, H. Puga et al., Additive manufacturing assisted investment casting: a low-cost method to fabricate periodic metallic cellular lattices. Addit. Manuf. **33**, 101085 (2020). https://doi.org/10.1016/j.addma.2020.101085

19. N. Wang, E. Maire, X. Chen et al., Compressive performance and deformation mechanism of the dynamic gas injection aluminum foams. Mater. Charact. **147**, 11–20 (2019). https://doi.org/10.1016/j.matchar.2018.10.013

20. K. Heim, F. García-Moreno, J. Banhart, Particle size and fraction required to stabilise aluminium alloy foams created by gas injection. Scripta Mater. **153**, 54–58 (2018). https://doi.org/10.1016/j.scriptamat.2018.04.041

21. D.K. Rajak, N.N. Mahajan, S. Das, Fabrication and investigation of influence of $CaCO_3$ as foaming agent on Al–SiCp foam. Mater. Manuf. Processes **34**(4), 379–384 (2019). https://doi.org/10.1080/10426914.2018.1532093

22. Y. Ma, X. Yang, C. He et al., Fabrication of in-situ grown carbon nanotubes reinforced aluminum alloy matrix composite foams based on powder metallurgy method. Mater. Lett. **233**, 351–354 (2018). https://doi.org/10.1016/j.matlet.2018.09.051

23. O. Andersen, H. Göhler, C. Kostmann et al., Powder metallurgically manufactured cellular metals from carat gold alloys for decorative applications. Met. Powder Rep. **73**(2), 72–79 (2018). https://doi.org/10.1016/j.mprp.2017.06.002

24. H. Jain, G. Gupta, R. Kumar et al., Microstructure and compressive deformation behavior of SS foam made through evaporation of urea as space holder. Mater. Chem. Phys. **223**, 737–744 (2019). https://doi.org/10.1016/j.matchemphys.2018.11.040

25. M. Vesenjak, M.A. Sulong, L. Krstulović-Opara et al., Dynamic compression of aluminium foam derived from infiltration casting of salt dough. Mech. Mater. **93**, 96–108 (2016). https://doi.org/10.1016/j.mechmat.2015.10.012

26. H. Puga, V.H. Carneiro, C. Jesus et al., Influence of particle diameter in mechanical performance of Al expanded clay syntactic foams. Compos. Struct. **184**, 698–703 (2018). https://doi.org/10.1016/j.compstruct.2017.10.040

27. C. Körner, M. Hirschmann, V. Bräutigam et al., Endogenous particle stabilization during magnesium integral foam production. Adv. Eng. Mater. **6**(6), 385–390 (2004). https://doi.org/10.1002/adem.200405147

28. K. Renger, H. Kaufmann, Vacuum foaming of magnesium slurries. Adv. Eng. Mater. **7**(3), 117–123 (2005). https://doi.org/10.1002/adem.200400191

29. D.H. Yang, B.Y. Hur, S.R. Yang, Study on fabrication and foaming mechanism of Mg foam using $CaCO_3$ as blowing agent. J. Alloys Compd. **461**(1–2), 221–227 (2008). https://doi.org/10.1016/j.jallcom.2007.07.098

30. G.L. Hao, F.S. Han, W.D. Li, Processing and mechanical properties of magnesium foams. J. Porous Mater. **16**(3), 251–256 (2009). https://doi.org/10.1007/s10934-008-9194-y

31. T.R. Neu, M. Mukherjee, F. Garcia-Moreno et al. Magnesium and magnesium alloy foams, in *7th International Conference on Porous Metals and Metallic Foams (MetFoam2011)* (2011), p. 133

32. Q. Fabrizio, A. Boschetto, L. Rovatti et al., Replication casting of open-cell $AlSi_7Mg_{0.3}$ foams. Materials Letters **65**(17–18), 2558–2561 (2011). https://doi.org/10.1016/j.matlet.2011.05.057

33. E. Aghion, Y. Perez, Effects of porosity on corrosion resistance of Mg alloy foam produced by powder metallurgy technology. Mater. Charact. **96**, 78–83 (2014). https://doi.org/10.1016/j.matchar.2014.07.012

34. L. Yilong, Q. Guibao, Y. Yang et al., Preparation and compressive properties of magnesium foam. Rare Metal Materials and Engineering **45**(10), 2498–2502 (2016). https://doi.org/10.1016/S1875-5372(17)30022-X

35. G.A. Lara-Rodriguez, I.A. Figueroa, M.A. Suarez et al., A replication-casting device for manufacturing open-cell Mg foams. J. Mater. Process. Technol. **243**, 16–22 (2017). https://doi.org/10.1016/j.jmatprotec.2016.11.041

36. A. Yánez, M.P. Fiorucci, A. Cuadrado et al., Surface roughness effects on the fatigue behaviour of gyroid cellular structures obtained by additive manufacturing. Int. J. Fatigue **138**, 105702 (2020). https://doi.org/10.1016/j.ijfatigue.2020.105702

37. A. Ataee, Y. Li, D. Fraser et al., Anisotropic Ti–6Al–4V gyroid scaffolds manufactured by electron beam melting (EBM) for bone implant applications. Mater. Des. **137**, 345–354 (2018). https://doi.org/10.1016/j.matdes.2017.10.040

38. C.N. Kelly, J. Francovich, S. Julmi et al., Fatigue behavior of As-built selective laser melted titanium scaffolds with sheet-based gyroid microarchitecture for bone tissue engineering. Acta Biomater. **94**, 610–626 (2019). https://doi.org/10.1016/j.actbio.2019.05.046

39. C. Yan, L. Hao, A. Hussein et al., Ti–6Al–4V triply periodic minimal surface structures for bone implants fabricated via selective laser melting. J. Mech. Behav. Biomed. Mater. **51**, 61–73 (2015). https://doi.org/10.1016/j.jmbbm.2015.06.024

40. G. Li, L. Wang, W. Pan et al., In vitro and in vivo study of additive manufactured porous Ti_6Al_4V

scaffolds for repairing bone defects. Sci. Rep. **6**(1), 1–11 (2016). https://doi.org/10.1038/srep34072

41. J. Walker, E. Harris, C. Lynagh et al., 3D printed smart molds for sand casting. Int. Metalcast. **12**, 785–796 (2018). https://doi.org/10.1007/s40962-018-0211-x

42. J. Thiel, S. Ravi, N. Bryant, Advancements in materials for three-dimensional printing of molds and cores. Int. Metalcast. **11**, 3–13 (2017). https://doi.org/10.1007/s40962-016-0082-y

43. C.M. Choe, S.H. Sok, W.S. Ri et al., Manufacture of plaster core mold for large oxygen plant components using fused deposition modeling (FDM). Int. Metalcast. (2021). https://doi.org/10.1007/s40962-020-00549-5

44. J. Wang, S.R. Sama, G. Manogharan, Re-thinking design methodology for castings: 3D sand-printing and topology optimization. Int. Metalcast. **13**, 2–17 (2019). https://doi.org/10.1007/s40962-018-0229-0

45. S. Singamneni, O. Diegel, D. Singh et al., Rapid casting of light metals: an experimental investigation using Taguchi methods. Int. Metalcast. **5**, 25–36 (2011). https://doi.org/10.1007/BF03355516

46. M. Antonelli, I. Knudson, A. Popernack et al., Cast aluminum mesostructures using 3D printed sand cores with an encapsulation. Int. Metalcast. **10**, 111–113 (2016). https://doi.org/10.1007/s40962-015-0011-5

47. H. Zhao, P.K. Nam, V.L. Richards et al., Thermal decomposition studies of eps foam, polyurethane foam, and epoxy resin (SLA) as patterns for investment casting; analysis of hydrogen cyanide (HCN) from thermal degradation of polyurethane foam. Int. Metalcast. **13**, 18–25 (2019). https://doi.org/10.1007/s40962-018-0240-5

48. Y. An, P.D. Hodgson, C. Yang, Investigation of cell shape effect on the mechanical behaviour of open-cell metal foams. Comput. Mater. Sci. **55**, 1–9 (2012). https://doi.org/10.1016/j.commatsci.2011.11.030